



Cite this: *EES Batteries*, 2026, **2**, 683

Coupling X-ray computed tomography with digital volume correlation to study core collapse in lithium-ion batteries

Kamel Madi, ^a Loic Courtois, ^a Luigi Raspolini, ^b Jinhong Min, ^c Amariah Condon ^c and Peter M. Attia ^c

This study investigates the link between internal cell features and mechanical behaviour of commercial cylindrical lithium-ion batteries (LIBs), which impacts both safety and performance. X-ray computed tomography is combined with digital volume correlation to study the core collapse mechanisms of LIBs during cycling. Detailed correlations between volumetric strain distribution and internal mechanical features, such as the positive tab, negative tabs, and kinks, were identified. Complex, heterogeneous swelling takes place within consistent vertical localised bands that correlate with the position of key internal features. The novel data analysis approach also provides insights into the changes in shape of the jellyroll during cycling. The heterogeneous deformation of the cells resulted in wrinkling and buckling of the jellyroll, which was reproduced and correlated to local tensile/compressive strains developing around the innermost layers. This approach can be used to understand the impact of cell design features on core collapse and provide strain data to validate numerical mechanical models.

Received 10th December 2025,
Accepted 5th February 2026

DOI: 10.1039/d5eb00229j

rsc.li/EESBatteries

Broader context

Commercial cylindrical lithium-ion batteries often experience “core collapse”—inward buckling of the wound electrode layers—which contributes to safety risks and abrupt capacity loss. Despite its importance, the 3D internal strain fields driving this failure mode are difficult to experimentally measure. In this work, we apply high-resolution X-ray computed tomography (CT) coupled with Digital Volume Correlation (DVC) to directly quantify the full-field 3D displacement and strain evolution inside commercial cells during cycling. Our study reveals that: large tensile strains form early around geometric inhomogeneities such as the positive tab and internal kinks. Heterogeneous vertical bands of expansion and contraction propagate inward from the casing toward the core as degradation progresses. Wrinkling and buckling of the jellyroll can be reproduced and quantitatively linked to compressive hoop strains and radial tensile strains. Inner negative tab displacement strongly correlates with the magnitude of inward expansion, providing a potential new indicator of core collapse progression. To our knowledge, this is the first experimental visualization and quantification of the 3D local strain directions responsible for wrinkling and buckling around the inner regions of a cylindrical cell. These insights can directly inform mechanical model validation, cell design improvements, and predictive manufacturing quality control.

1. Introduction

Lithium-ion batteries are used extensively in modern life.^{1–3} As a lithium-ion battery cell ages, its electrode layers swell due to both reversible (*e.g.*, negative electrode volumetric expansion during intercalation) and irreversible (*e.g.*, the buildup of side reaction products) processes.³ This swelling can lead to a high-risk failure mode in wound cells (as opposed to stacked cells), which have a central void region from the winding process; specifically, if the jellyroll is constrained (*e.g.*, due to a rigid

case or external pressure), the jellyroll will swell inwards towards the core to relieve the additional stress induced from the swelling. This swelling-induced stress often results in buckling of the jellyroll (sometimes termed “core collapse” in cylindrical cells),⁴ which itself can lead to both a “knee” (a sudden & sharp decrease) in capacity/energy and internal shorting due to separator tears and/or lithium plating.

Core collapse in cylindrical cells has been extensively studied.^{4–13} The archetypal core collapse study involves periodic computed tomography (CT) scanning of a cylindrical cell over the course of a cycling experiment to monitor the progression of buckling with aging.¹⁴ CT scanning can nondestructively¹⁵ reveal the internal structure of a cell in 3D with micron-scale resolution and is thus an excellent technique for studying cell mechanical behaviour. That said, a key input for

^a3Dmagination Ltd, Building R70, Rutherford Appleton Laboratory, Harwell Campus, Didcot OX110QX, UK. E-mail: kamel.madi@3dmagination.uk

^bThermoFischer Scientific, Eindhoven, Netherlands

^cGlimpse, 444 Somerville Avenue, Somerville, Massachusetts 02143, USA



understanding and modelling cell mechanical behaviour is the evolution of 3D strain within the bulk of the cell. Acquiring this dataset requires transforming CT reconstructions into 3D strain maps. Virtual electrode unrolling techniques provide a deeper view inside the electrode layers. The “unrolled” maps allow for quantitative analysis and visualization of mechanical changes (electrode expansion/contraction) and strain distribution.^{6,16–18} However, the strain maps are measured in 2D from the change in position of the electrode roll contours,

which differs from the deformation within the bulk of the cells. Digital Volume Correlation (DVC) is a powerful technique to measure 3D full-field displacement and strain maps at the continuum-level from volume images acquired during the deformation process of materials.¹⁹ Although DVC has been previously used to guide the development of more effective cell designs,^{6–8} the technique still has more to offer to better understand the mechanisms driving core collapse initiation and progression.^{4,12,16,20–26} In particular, many questions still remain about how cell-level geometric inhomogeneities cause non-uniform stress–strain distributions leading to mechanical degradation around the inner core. Additionally, this 3D strain data is critical for validating cell mechanical models of this phenomenon.

This study highlights the utility of high-throughput, high-resolution CT coupled with DVC for understanding cell mechanical behaviour. Periodic CT scans are performed to monitor the progression of core collapse during cycling in five commercial cylindrical cells with various initial buckling states. A sophisticated approach is used to link the internal strains to the positive/negative tabs, internal defects (kinks), and inner core. A new approach for tracking the changes in jellyroll shape is proposed to explore the mechanisms initiating

Table 1 Information on the five cells used in this study

Sample ID	Producer	Cell model	Mean inner/outer diameter (mm)	Mean can wall thickness (mm)	Number of buckled cathode layers† at BOL
LIB09	VapCell	F56	21/21.5	0.458	3
LIB15	VapCell	F56	21/21.5	0.459	2
LIB18	VapCell	F56	21.1/21.5	0.455	1
LIB20	VapCell	F56	21.1/21.5	0.459	0
LIB25	VapCell	F56	21.1/21.5	0.450	3

†The number of buckled cathode layers includes the thin tapered cathode layer.

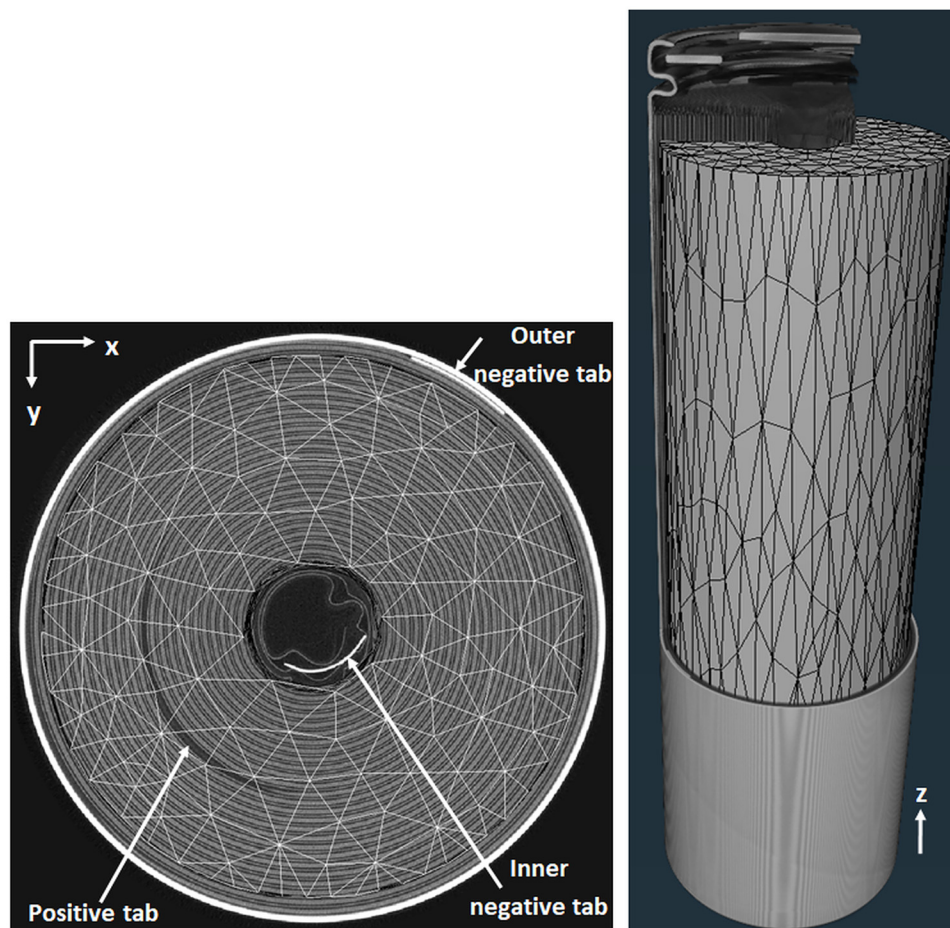


Fig. 1 3D tetrahedral mesh of the jellyroll. The region around the casing was excluded from the analysis due to the abrupt change of grey level.



core collapse around the inner core (wrinkling/buckling), and the data are correlated to the magnitude and direction of the strains around the innermost layers. The expansion of the inner layers is also linked to the internal motion of the inner negative tab to investigate the progression of core collapse. The approach illustrated in this work can be used to understand the impact of cell design features on core collapse and provide strain data to validate numerical mechanical models.

2. Materials and methods

2.1. Experimental protocol

2.1.1. Cell selection. Five cells were used in this study (Table 1). The cells are marketed as “VapCell” F56 cells with a nominal capacity of 5600 mAh. We selected five cells from a population of 25 cells scanned in Condon *et al.*¹⁴ to obtain a diversity of buckling states at BOL. The mean inner diameter, mean outer diameter, mean can wall thickness, and the number of buckled cathode layers at beginning-of-life (BOL) were all quantified *via* CT.

2.1.2. Computed tomography. The CT scans are performed by Glimpse at their facility in Somerville, MA, USA. The CT

scanning parameters are identical to Condon *et al.*,¹⁴ except the exposure was four times as long to reduce noise. Min *et al.*¹⁵ confirmed that lab-scale X-ray exposure does not harm cell performance or lifetime, so we can confirm the electrochemical results are unaffected by the X-ray experiments.

2.1.3. Cell cycling. The cell testing procedure consisted of running a cycling protocol with periodic interruptions for CT scanning and a reference performance test (RPT). The CT scans and RPTs occurred at cycles 0, 50, 100, 200, and 350, after which the experiment was stopped due to safety concerns (the cells exhibited high self-discharge rates). Below, 1C represents the current required to charge or discharge the cell in 1 hour, which is 5600 mAh.

For the cycling tests, all cells were charged at a constant current of 2000 mA (C/2.8) until they reached a cutoff voltage of 4.2 V, after which the voltage was held until the charging current dropped to 100 mA. Discharging was conducted at a constant current of 11.2 mA (2C) until the cells reached a cutoff voltage of 2.5 V. Cycling tests were performed in convection-based temperature chambers set to 45 °C to accelerate cell aging.

The RPT test consisted of three consecutive constant charge and discharge cycles as well as an open-circuit voltage (OCV) decay test. In the first cycle, the cells were charged at a con-

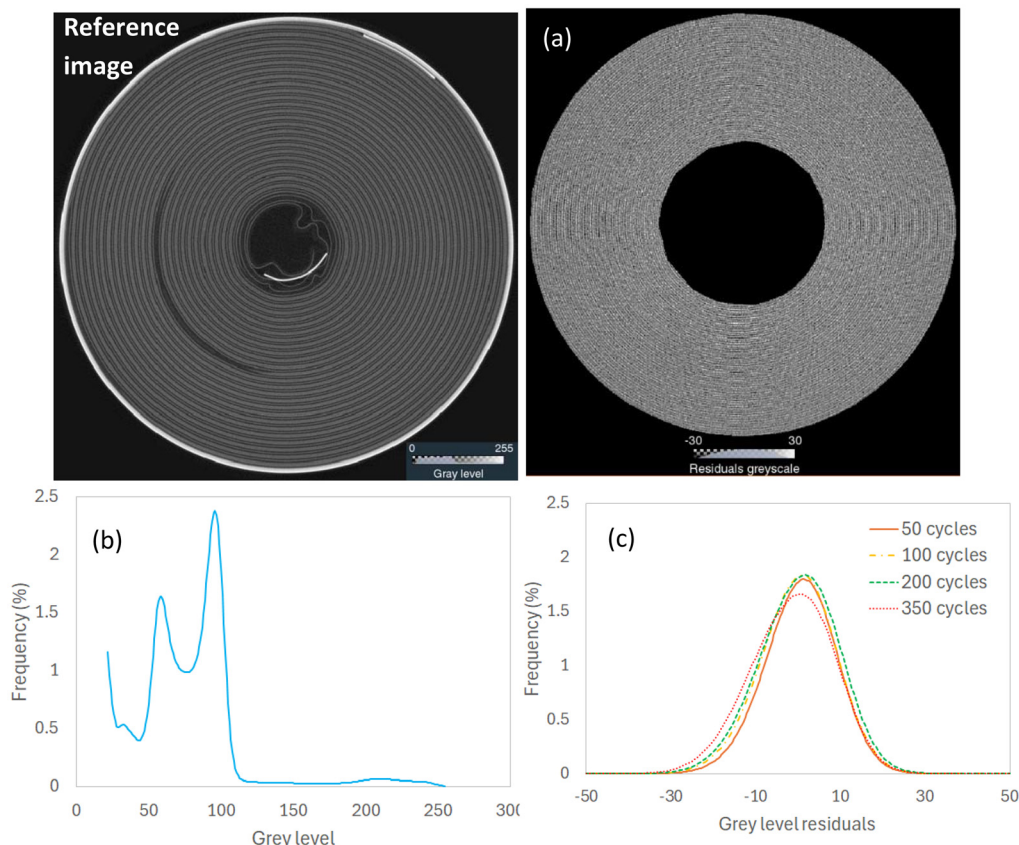


Fig. 2 (a) Correlation residuals image obtained after 50 cycles. Comparison between the grey level histogram obtained from the reference image (b) and the correlation residuals histograms obtained at each cycle (c). After subtracting the reference image from the deformed images corrected by the displacement field, only noise and artefacts remain in the correlation residuals image.



stant current of 280 mA (C/20) until they reached a cutoff voltage of 4.2 V and then discharged at 280 mA to a cutoff voltage of 2.5 V. In the second cycle, the cells were charged at 1120 mA (C/5) to 4.2 V and then discharged at 1120 mA to 2.5 V. In the third cycle, the cells were charged at 2800 mA (C/2) to 4.2 V and then discharged at 2800 mA to 2.5 V. A five-minute rest period was included between each cycle. Lastly, the OCV decay test consisted of a 0.1C charge to 4.2 V, an OCV decay observation period of 48 hours, and then a 0.1C discharge to 2.5 V. The tests were conducted in convection-based temperature chambers set to 33 °C; conventionally, RPT tests are performed at, or slightly above, room temperature to understand the state of the cell in field-representative conditions.

2.2. Digital volume correlation (DVC)

2.2.1. DVC global approach. A robust DVC strategy implemented in the XDigitalVolumeCorrelation module of Avizo 3D Pro^{27,28} was employed to compute the displacements and strains of the LIB cells at different cycles. A Finite Element unstructured mesh composed of four-node tetrahedrons with first-order shape functions (T4 elements) was generated from a binary mask of the jellyroll (Fig. 1) and used to measure the DVC displacements. A global finite element (FE)-based correlation algorithm was applied, whereby the whole volume of interest is analysed and the displacement is obtained by minimising ρ_c^2 the sum of squared differences between the reference and deformed images over the region of interest (ROI):

$$\rho_c^2 = \int_{\text{ROI}} \varphi_c^2(x) dx, \quad (1)$$

where

$$\varphi_c(x) = f(x) - g(x+u(x)), \quad (2)$$

also known as the correlation residuals.^{28,29} To solve this non-linear problem, a Gauss–Newton iterative procedure is applied which can be expressed as a matrix inversion problem:²⁹ $M\{\delta u\} = b$, with M being the problem matrix, δu the sought increment of displacement at the considered increment, and b the second member (depending on the image gradient of the reference image and the correlation residual). M being constant, the resolution of the DVC problem consists in successive updates of the second member b after each iteration. The algorithm converges when the displacement increment norm $|\delta u|$ is smaller than 0.001 voxels, which means the displacement field $u(x)$ has been correctly measured. The nodal displacements are interpolated using the shape functions of the T4 elements. A trilinear interpolation is used to achieve registration at the sub-voxel level. The derivatives of the displacements with respect to the mesh were used to calculate the deformation gradient and all the components of the Green–Lagrange strain tensor without additional smoothing. The anti-symmetric part of the strain tensor was also extracted to quantify the local, in-plane rotation of the jellyroll (x – y plane).

2.2.2. DVC strategy of the deformed images. The DVC analysis of the LIB cells is a difficult task due to the complex, peri-

odic microstructure of the jellyroll. The current collectors, cathode, separator and anode are wound around the central supportive core, forming periodic layers in the radial and axial directions of the jellyroll (axial direction corresponds to the z axis, *i.e.* along the cylinder's length). These periodic patterns can lead to secondary minima when solving the correlation problem, which can make it difficult for the DVC algorithm to converge.³⁰ To address this issue, three important steps were implemented.

First, the deformed XCT datasets were registered to the reference CT image using registration techniques to suppress the rigid body motion. During the registration, the data were aligned to the negative and positive tabs of the reference image. This allowed the CT scans to remain as close as possible before the DVC analysis.

Second, since the deformation of the jellyroll is often described as occurring predominantly in the radial and hoop directions during cycling,^{4,31} the axial displacements were not investigated and our DVC study focused essentially along the radial and hoop directions (x – y plane). This was achieved by reducing the spatial resolution of the DVC measurements along the cylinder height, allowing nonetheless to capture the rigid body axial displacements. Therefore, an anisotropic mesh with T4 elements of size 120 voxels (~ 2 mm) along the

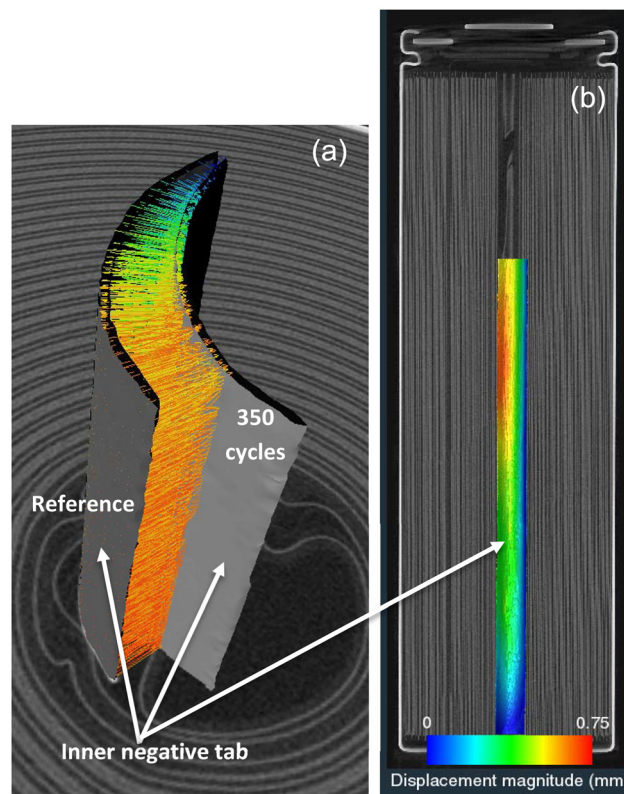


Fig. 3 Tracking the displacement vectors of the inner negative tab surface obtained from the registered CT scans: (a) displacement vectors and (b) displacement magnitude mapped onto the surface of the inner negative tab. This method can capture the heterogeneous displacement of the inner negative tab as a result of the inward expansion of the inner layers.



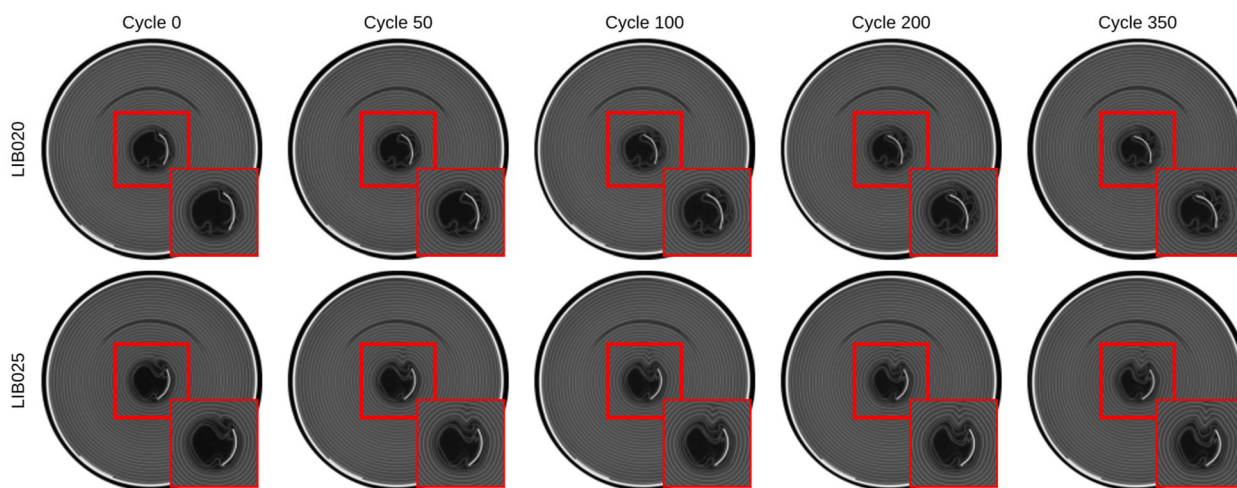


Fig. 4 Progression of core collapse in cells LIB020 and LIB025 as a function of cycle number via CT scans. The CT scans were obtained after 0, 50, 100, 200, and 350 cycles. The images were computationally aligned to the positive tab for visual consistency. A single slice obtained from the middle of the primary axis of the cell (*i.e.*, $Z = 35$ mm) was extracted from each scan. The core collapse becomes increasingly severe as a function of cycle number, although the core collapse in LIB025 is substantially more severe than that in LIB020.

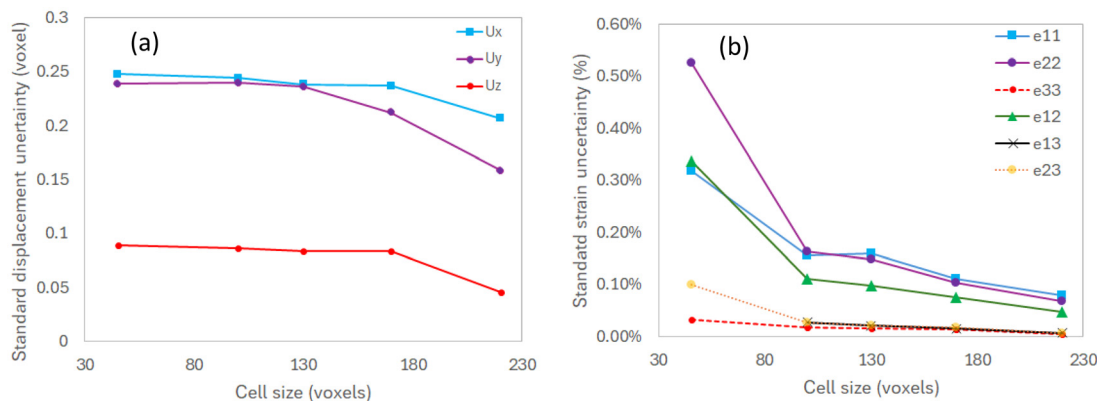


Fig. 5 Standard displacement and strain uncertainties versus cell size: (a) displacement components (unit: voxel, voxel size: $16.4 \mu\text{m}$), (b) strain components.

radial direction (x - y plane) and 360 voxels (~ 6 mm) along the axial direction (z axis) was used (Fig. 1). The cubic root of the mean volume of the T4 elements, defined as an equivalent length, is about 85 voxels which is ~ 5 - 6 times the size of the anode/cathode layers. At this scale of observation, DVC is primarily used for continuum-level analysis of the jellyroll. Resolving the strains within the layers would require the mesh size to be very small (*i.e.* close to the voxel size) which can dramatically amplify errors (*i.e.* noisy displacements) and the matrix M may no longer be invertible.

Third, the maximum sought displacement between two scans after registration (< 6 - 7 voxels, *i.e.* $\sim 100 \mu\text{m}$) was usually smaller than the correlation distance of the jellyroll (~ 10 - 15 voxels, 150 - $250 \mu\text{m}$); the correlation distance is dependent upon the arrangement/size of the anode/cathode and tabs, and was measured using the autocorrelation function in Avizo. Therefore, a large strain incremental approach was used to keep the scans

within correlation distance. The DVC computations were internally performed on consecutive images (reference-50 cycles, 50 cycles-100 cycles, 100 cycles-200 cycles, 200 cycles-350 cycles)

Table 2 DVC results in response to applied macroscopic strain

	$\langle e_{xx} \rangle$	$\langle e_{yy} \rangle$	$\langle e_{zz} \rangle$
Applied strains 1	1%	1%	0
DVC	0.94%	0.94%	0
Applied strains 2	1%	1%	0.5%
DVC	0.99%	0.97%	0.54%
Applied strains 3	1%	1%	1%
DVC	0.95%	0.94%	0.94%
Applied strains 4	2%	2%	0
DVC	1.87%	1.91%	0
Applied strains 5	2%	2%	0.5%
DVC	1.87%	1.85%	0.44%
Applied strains 6	2%	2%	1%
DVC	2%	1.99%	0.92%



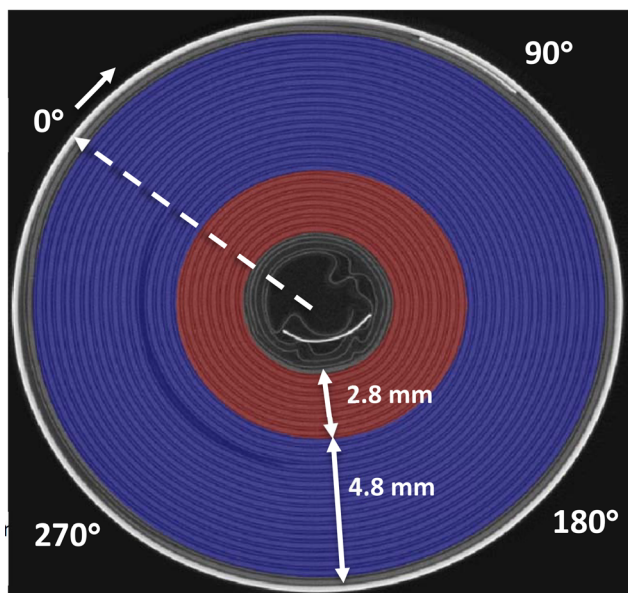


Fig. 6 Definition of the inner/outer layers and reference axis for the rotation angle of the cell.

and the reference mesh was deformed on each step by the displacement field of the previous step. The total displacement at each step was obtained by summing the previous displacements and computing the corresponding strain tensor onto the original reference mesh.³² When larger displacements were observed between the first step (50 cycles) and reference, the displacements obtained on a coarser mesh (mesh size: 220 voxels) were used as a guess to initialise the DVC analysis on the reference mesh (mesh size: 120 voxels).

All the DVC analyses were performed using a laptop with 8-cores processor running at 2.3 GHz and a RAM at 128 GB. The DVC calculations converged successfully after 50–200 iterations, necessary to solve the matrix inversion problem. To validate that the algorithm converged to a meaningful value of the displacement field, it is recommended to check that the correlation residuals image are limited to the imaging noise.²⁹ Fig. 2 demonstrates that after subtracting the reference image from the deformed images corrected by the displacement field, only noise and artefacts remain in the correlation residuals image. This indicates a good correlation quality, leaving only a Gaussian distribution of noise/artefacts with grey levels standard deviation between ± 8 –10. The presumed

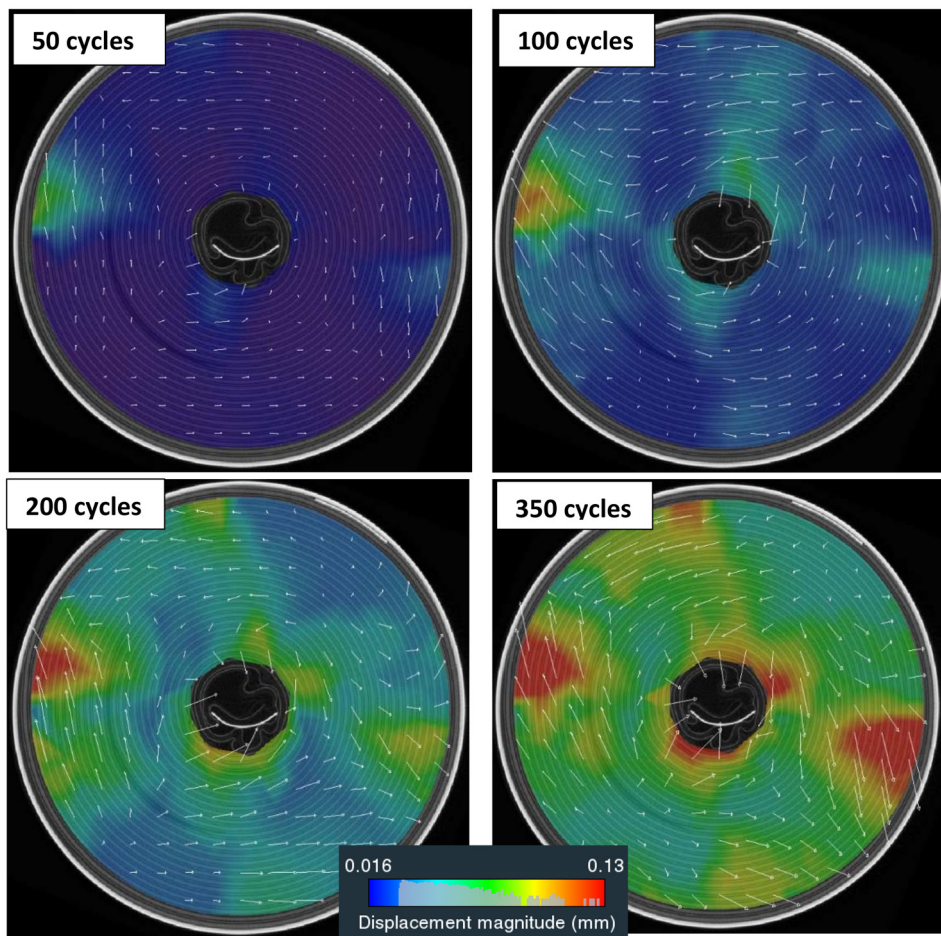


Fig. 7 Evolution of the displacement vectors and displacement magnitude at mid-section during cycling for LIB20. Large displacements concentrate between the casing and the positive tab and around the innermost layers where they gradually spread within bands along the radial direction.



noise/artefact level was calculated as the standard deviation of the correlation residuals divided by the dynamic range of the reference image.^{27,28} For each loading step, this level reached about 3.5% and remained very close to the level observed in the repeat scan analysis for which no strains occurred. Therefore the DVC results are deemed trustworthy.

2.2.3. Displacement and strain uncertainties. In DVC, standard displacement (resp. strain) resolution and spatial resolution always exhibit an inverse relationship.³³ The spatial resolution is defined as the size of the interrogation window (or element size). Since the aim of this study was to determine the measurement uncertainty associated with the jellyroll architecture, the method applied in this work consisted of correlating two consecutive CT scans in the unloaded state (often called repeat scans) as a function of the element size.^{29,34} This procedure takes into account the noise level associated with the CT scanner equipment, acquisition parameters and the applied reconstruction algorithm. The acquisition noise level is expected to be approximately the same since the same acquisition parameters were applied to the five CT scans. In this work, only one CT scan was acquired in the unloaded state. After performing the DVC analysis of step 1 (reference vs. 50 cycles), a repeat scan was created by simply adding the noise level to the reference scan using eqn (2). The analysis consisted of correlating the two repeat scans as a function of the element size. The mesh size along the radial direction was varied between 45 and 220 voxels (0.7–3.6 mm) with increments of 40 voxels (0.65 mm), while the mesh size along the z direction was fixed to 360 voxels (~6 mm). The standard displacement and strain uncertainties, referred to as standard displacement and strain resolutions, were measured from the standard deviation of the displacement and strain fields, respectively, relative to their mean values.

2.2.4. Performance evaluation. New artificial volumes were also constructed from the reference image to investigate the performance of the DVC algorithm to a prescribed macro-

scopic strain.^{27,33} In Avizo, it is possible to define complex transformations consisting of an arbitrary number of basic transformations (translations, rotations, normal strain, shear, etc.). The method consisted in deforming the reference image by applying consecutive uniform strains of 1% along the radial

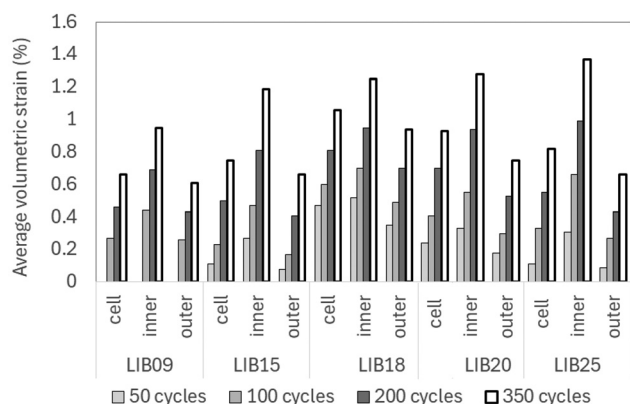


Fig. 8 Average volumetric strain across the cells vs. number of cycles. The 'inner' and 'outer' values represent the average strains measured over the inner and outer layers represented in Fig. 6, while 'cell' denotes the average strain calculated over the entire jellyroll. The swelling of the inner layers is typically 1.5x to 3.5x the swelling of the outer layers.

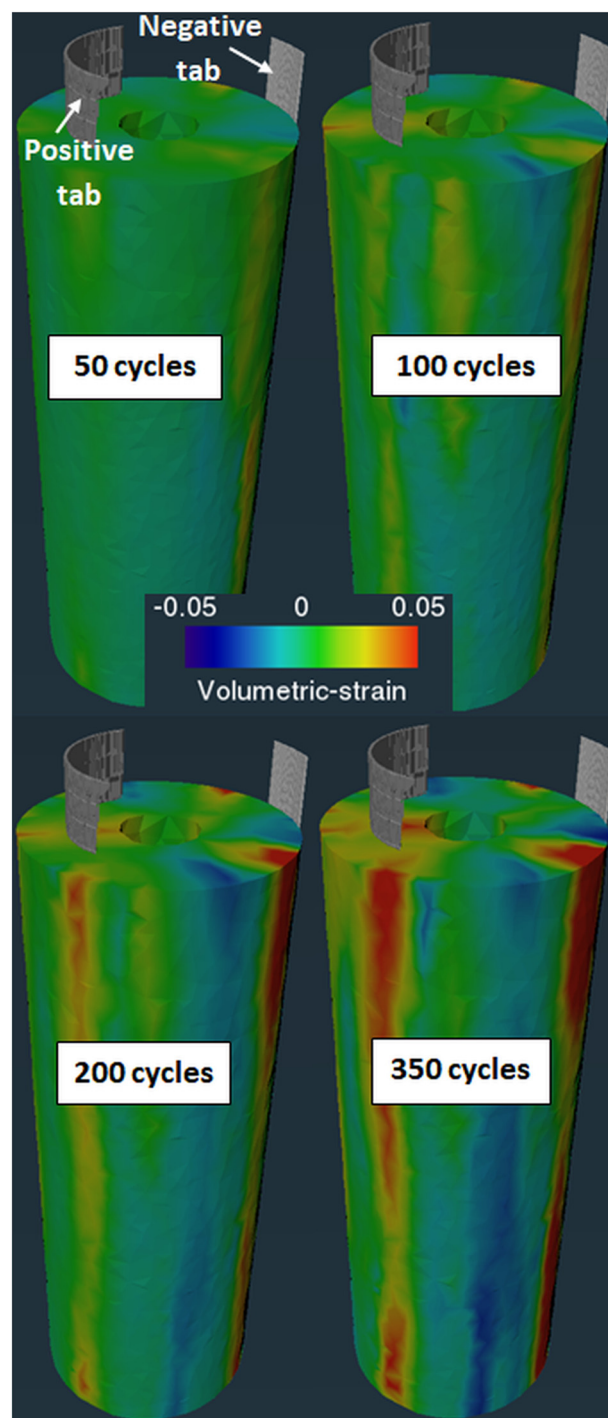


Fig. 9 Evolution of volumetric strain across LIB20 during cycling. Vertical bands of high expansion seem to consistently initiate and develop around the positive tab and inner core, and are further followed during cycling by alternating bands of expansion (yellow-red shade) and contraction (cyan-blue shade).



direction. This strain magnitude was close to that measured from the real images. Although the axial strains in the real images were usually negligible, small strain steps of 0.5% were also applied along the axial direction to test the performance of the DVC algorithm. The systematic error was calculated from the difference between the spatial average of the measured and the prescribed strains.

2.3. Jellyroll shape changes

To further enhance the understanding of the core collapse mechanisms, the DVC results were also used to track the changes in jellyroll shape during cycling. For each CT scan, a binary mask of the jellyroll inner coils was used to generate a surface mesh using the Marching Cubes algorithm implemented in Avizo. The surface mesh was then deformed by the corresponding displacement field obtained by DVC and converted to a binary image to provide a voxel-based representation. The displacement field was amplified by a factor of 10 to magnify the shape change. The

coordinates of the binary mask were converted to a spreadsheet and plotted against cycle number.

2.4. Measurement of inner negative tab motion

The inner negative tab is welded to the inner layers of the jellyroll to create a secure electrical connection to the battery's internal structure. The displacement of the inner negative tab can be a sign of compromised structural integrity and could be used to track the progression of core collapse. The inner negative tab was segmented from the registered XCT datasets using a region growing algorithm and converted to surface meshes (Fig. 3a). The displacement vectors of the inner negative tab were calculated in Avizo by computing the local Euclidean distance between the deformed and the reference surfaces (*i.e.* 50 cycles *vs.* ref, 100 cycles *vs.* ref, *etc.*). The displacement magnitude was then mapped onto the surface of the inner negative tab (Fig. 3b) and the data was used to calculate the average displacement of the inner negative tab as a function of the cylinder height.

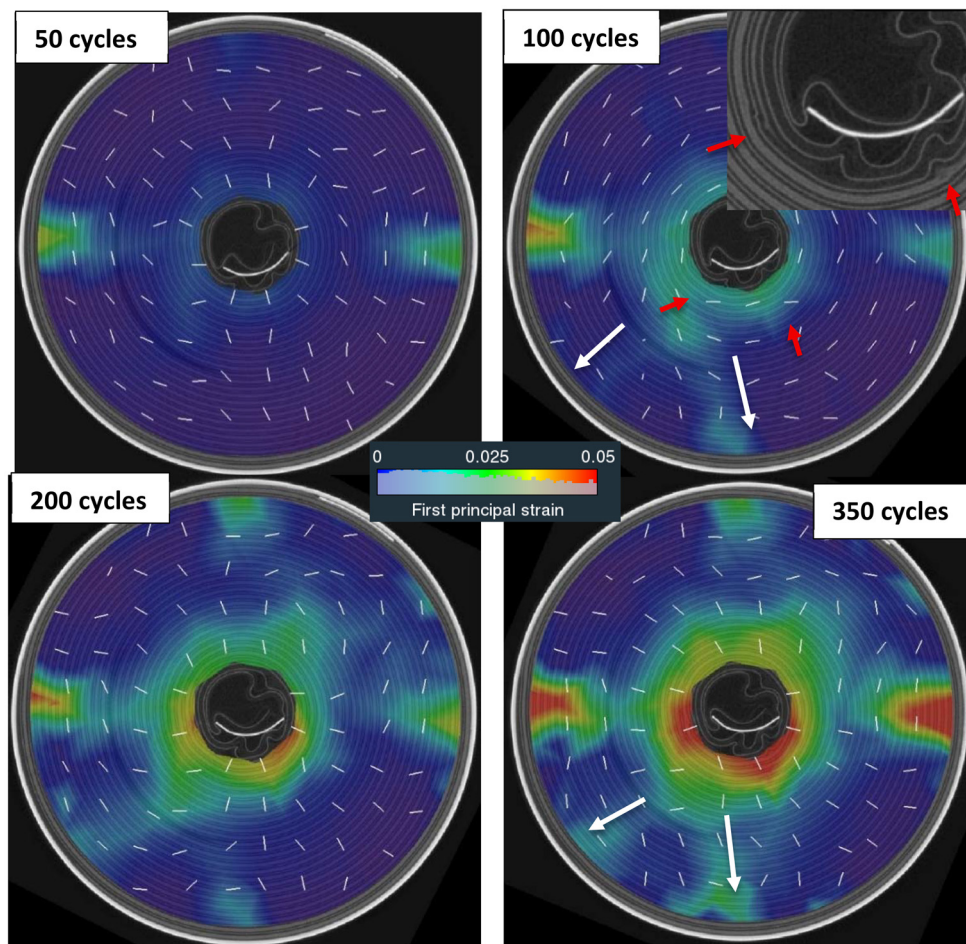


Fig. 10 Evolution of the first principal strain (tensile) at mid-section during cycling of LIB20. The white line segments indicate the principal directions associated to the tensile strains. Large tensile strains initiate near and opposite the positive tab, and around the innermost layers. From 100 cycles, a small local distortion of the jellyroll is visible around the innermost layers (red arrows) which was not present at BOL. These distortions seem to trigger two small bands of tensile strain spreading radially in the direction of the positive tab (white arrows). In the outer layers, the bands of large expansion (red) form along the hoop direction (white lines). Around the innermost layers, the inward expansion develops along the radial direction (white lines).



3. Results

3.1. Time-lapse XCT imaging

Fig. 4 displays the progression of core collapse in cells LIB020 and LIB025 as a function of cycle number. At cycle 0, the innermost cathode wraps of cell LIB020 appear pristine, while one cathode wrap has already buckled in cell LIB025. In both cases, the core collapse becomes increasingly severe as the cells continue cycling, although the core collapse in LIB025 is substantially more severe than that in LIB020. In LIB025, the core collapse occurs at the same angular position as the positive tab.

3.2. Digital volume correlation

3.2.1. Measurement uncertainties from repeat scans. The displacements and strain uncertainties as a function of the mesh size are reported in Fig. 5. As expected, the standard deviations of displacement and strain decrease when the mesh

size increases. These results highlight the inherent compromise between displacement uncertainty and spatial resolution that must be considered in DVC.^{27,29} For this study, a mesh size of 120 voxels along the x - y plane was chosen, which gives a displacement precision smaller than 0.25 voxel and a strain precision smaller than 0.15%. This is sufficient to accurately capture the local deformation inside the jellyroll, where local strains can reach up to 1–2% locally between two scans, and up to 10% when cumulated over 350 cycles. It is also observed that the displacement and strain uncertainties are smaller along the axial direction, which is explained by the larger mesh size along the z direction. This means that rigid axial displacements can be accurately captured during the correlation process.

3.2.2. Performance evaluation to prescribed displacement. The systematic errors as a function of the prescribed macroscopic strain are reported in Table 2. The systematic errors remain always smaller than 6–8% along the radial and axial

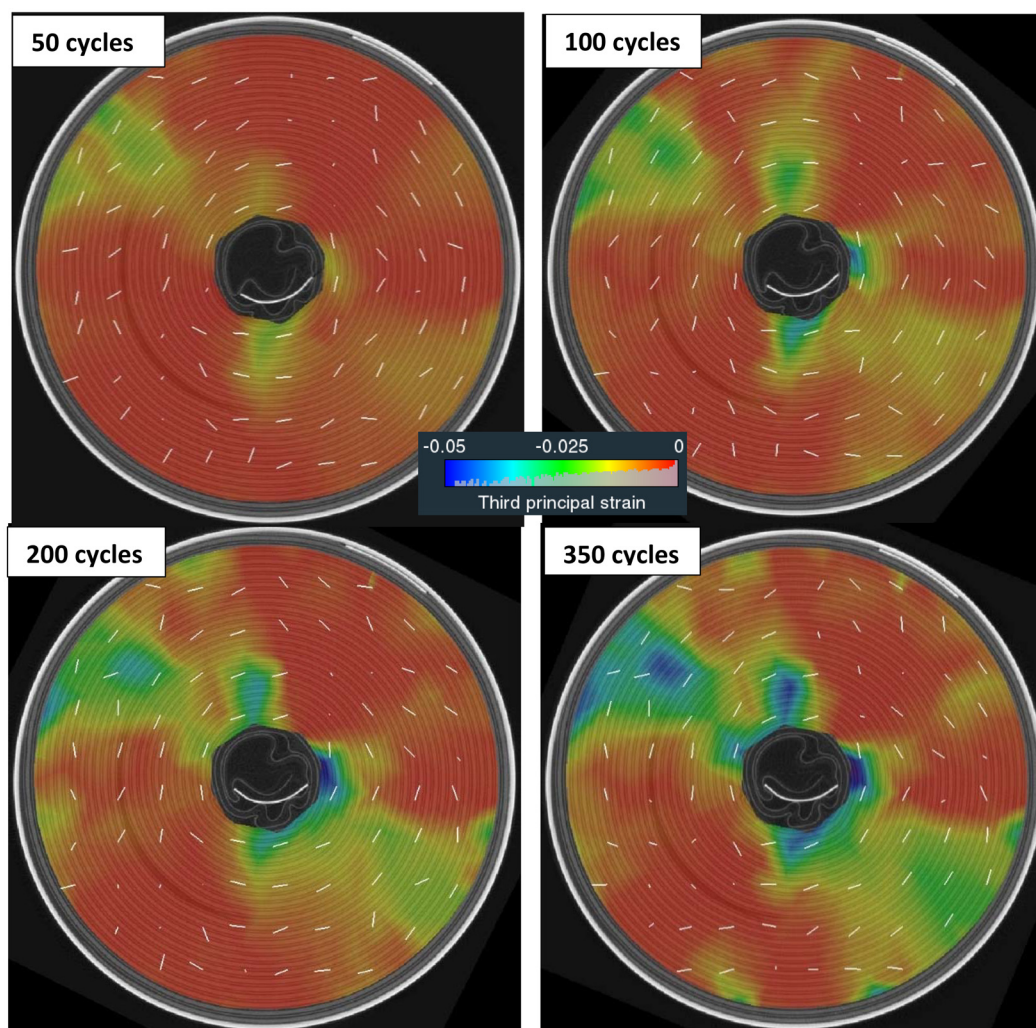


Fig. 11 Evolution of the third principal strain (compression) at mid-section during cycling of LIB20. The white line segments indicate the principal directions associated to the compressive strains. On each side of the positive and outer negative tabs, the outer jellyroll is subjected to compression, mostly along the hoop direction (white lines), extending to the inner core.



directions, which is satisfactory. The DVC algorithm is based on a FE approach where the continuity of the displacements is ensured, which leads to robust and accurate results.²⁷

3.2.3. Deformation mechanisms of the jellyroll during cycling. In this section, the DVC data are used to understand the macroscopic and local deformation of the jellyroll across the inner 7 layers (red colour), outer 15 layers (blue colour) and entire cell (Fig. 6). The strain maps of the inner layers are also linked to the changes in jellyroll shape and the motion of the inner negative tab.

In the following, the bulk strains (or volumetric strains) are used to track the swelling of the jellyroll and the principal strains (eigenvalues of the strain tensor) are exploited to decorelate the tensile regions from the compressive regions. In this study, except for LIB15 at 50 cycles, the first principal strain was always positive while the third principal strain was always negative (Fig. 12 and S12–S15). Therefore, the first principal strains result in elongation of the jellyroll and will be denoted as ‘tensile strains’ (indicated by a positive value) while the third principal strains cause compression and will be

designated as ‘compressive strains’ (indicated by a negative value). The directions associated with the first and third principal strains are also visualised to better clarify the deformation modes. The average tensile and compressive strains are plotted as a function of both height and rotation angle of the cell (the 0° reference axis is depicted in Fig. 6).

Displacement vectors and local rotation of the jellyroll. The results across the different cells were overall consistent. For simplicity, only LIB20 and LIB25 cells were selected to visualise the displacement maps inside the jellyroll. The evolution of the displacement vectors and displacement magnitude of LIB20 and LIB25, during cycling, are depicted in Fig. 7 and S1. The results obtained on the remaining cells are available in the SI Appendix. During cycling, heterogeneous displacements develop inside the jellyroll. After 50 cycles, it is observed that the displacement of the jellyroll initiates between the casing and the positive tab around the 0° line. Large displacements concentrate in this area and around the innermost layers where they gradually spread within bands along the radial direction, reaching up to 0.25 mm locally after 350 cycles. Around the inner core, the displacement

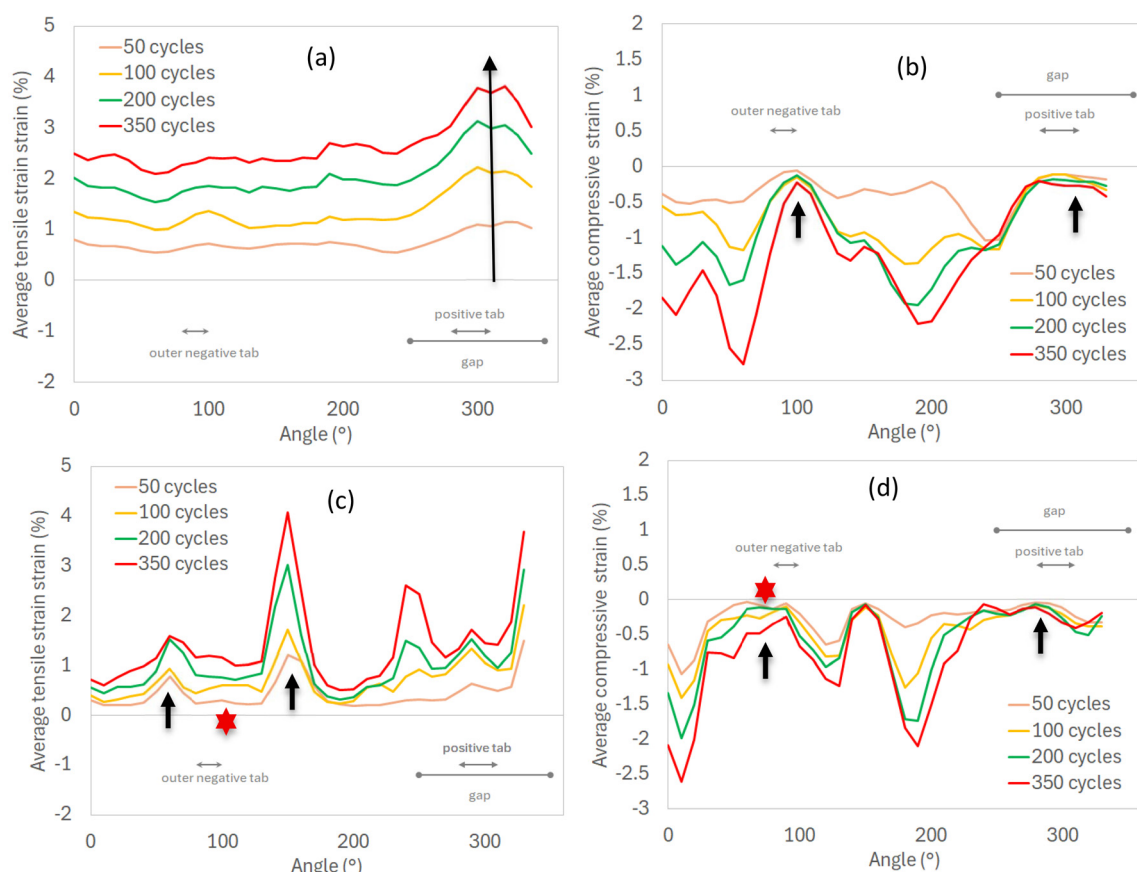


Fig. 12 Average strain of LIB20 as a function of the rotation angle of the cell: (a) tensile strain (inner layers), (b) compressive strain (inner layers), (c) tensile strain (outer layers), (d) compressive strain (outer layers). At 50 cycles, large tensile strains initiate around the innermost layers in the direction of the positive tab (dark arrow in a), and simultaneously tensile bands form in the outer layers on each side of the outer negative tab (dark arrows in c). During cycling, these bands grow further and new bands form. Around the positive and outer negative tabs, the compression is negligible in the inner/outer layers (dark arrows in b and d). On each side of the positive and outer negative tabs, the inner and outer layers are subjected to large compression (b and d). The lowest deformation (both tension/compression) is observed around the outer negative tab (red stars in c and d).



vectors are inwards. When progressing from the inner layers to the outer layers, the displacement vectors gradually point outward and, as a result, clock-wise and anti-clock wise rotation develop along the x - y plane (Fig. 7 and S2) with a maximum rotation observed along the 0° line.

Swelling of the jellyroll. The average volumetric strain, indicative of the macroscopic swelling, across the inner layers, outer layers and entire jellyroll of the different LIB cells are represented in Fig. 8. Although the results are slightly different between the different LIB cells due to the variability of the micro-structure, the macroscopic swelling of the cells are found to be proportional to the number of cycles, following the same linear relationship: $y = 0.002 \times x + y_0$ ($R^2 = 0.97$), where x is the number of cycles, y denotes the corresponding macroscopic swelling, and y_0 is the macroscopic swelling reached after 50 cycles. Also, depending on the LIB cell, the swelling of the inner layers is typically $1.5\times$ to $3.5\times$ the swelling of the outer layers.

Heterogeneous swelling develops locally inside the LIB cells as depicted by the 2D/3D maps of the volumetric strain in Fig. 9 and S3. At first glance, vertical bands of high expansion seem to consistently initiate and develop around the positive

tab and inner core, and are further followed during cycling by alternating bands of expansion and contraction. Locally, the swelling can reach up to 4% after 50 cycles and 15% after 350 cycles. In the next section, the tensile strains (expansion) are decorrelated from the compressive strains (contraction) and plotted as a function of the rotation angle of the cell to better characterize the radial and angular positions of the vertical bands during cycling.

Distribution of tensile and compressive strains. The distribution of the tensile and compressive strains of LIB20 and LIB25 at mid-section are illustrated in Fig. 10, 11 and Fig. S4, S5. The principal directions are superimposed to the strain maps using white line segments. The curves representing the average tensile and compressive strains as a function of the rotation angle of the cell are also shown in Fig. 12 and S15. The principal strain maps and curves of the remaining cells are available in the SI Appendix.

A different mechanical response is observed between the inner and outer layers.

Inner layers. Within the inner layers, regardless of the cell condition at BOL, high tensile strains localize preferentially

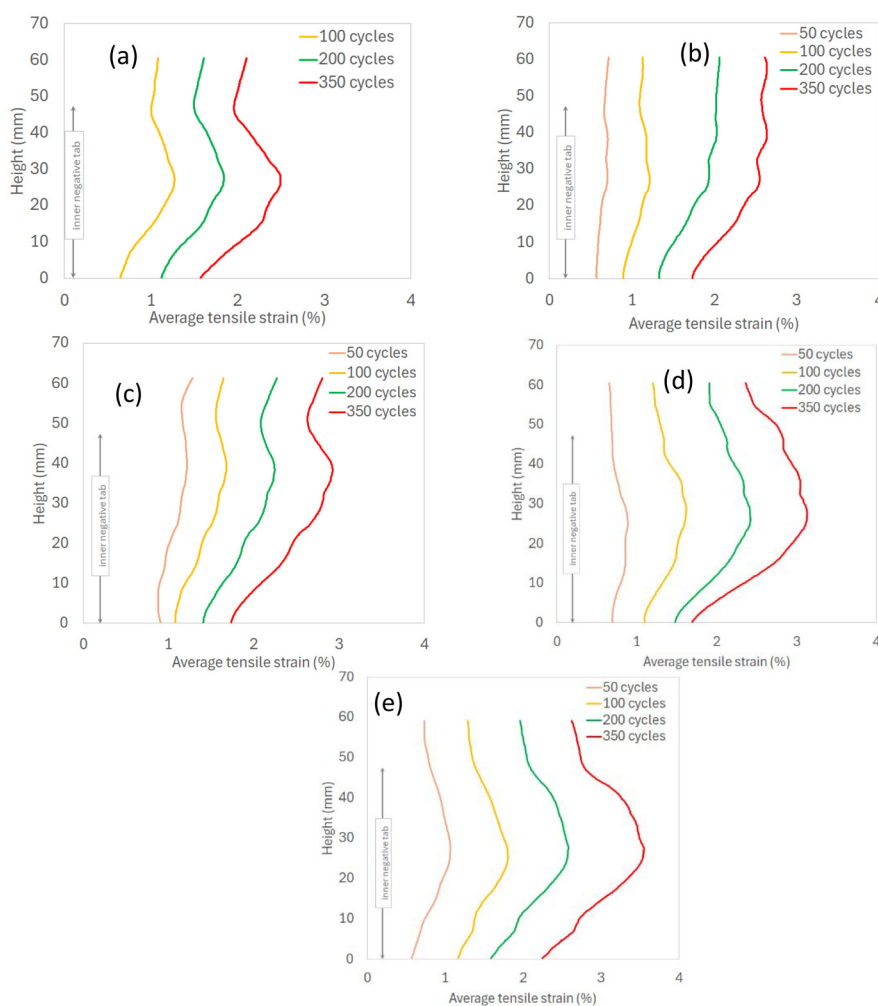


Fig. 13 Average tensile strain of the inner layers along cell height: (a) LIB09, (b) LIB15, (c) LIB18, (d) LIB20, (e) LIB25.



around the innermost layers where the inner core is free to expand. The expansion is 3% on average and up to 10–15% locally (Fig. 10, 12a and S4, S6, S8, S10, S12a–15a). Except LIB20, the tensile strains reach a maximum around the buckled layers present at BOL, forming kinks (Fig. S4, S6, S8 and S10). As the number of cycles increases, the kinks deform and grow further, accumulating more deformation. Away from the kinks, the tensile strains seem to develop more uniformly over the inner six layers. In LIB20, the tensile strains of the inner layers are maximum along the direction of the positive tab (Fig. 12a). Two small distur-

tions of the jellyroll are visible from 100 cycles (not present at BOL, red arrows in Fig. 10) and seem to initiate two small bands of tensile strain spreading radially in the direction of the positive tab (white arrows in Fig. 10). In all the cells, the innermost layers are also subjected early to highly localized compressive strains, -3% on average and down to -10% locally (Fig. 11, 12b and S5, S7, S9, S11, S12b–15b). More importantly, around the inner core, the principal directions indicate that the tensile strains build up essentially along the radial direction while the compressive strains develop along the hoop direction (Fig. 10, 11 and S4, S5).

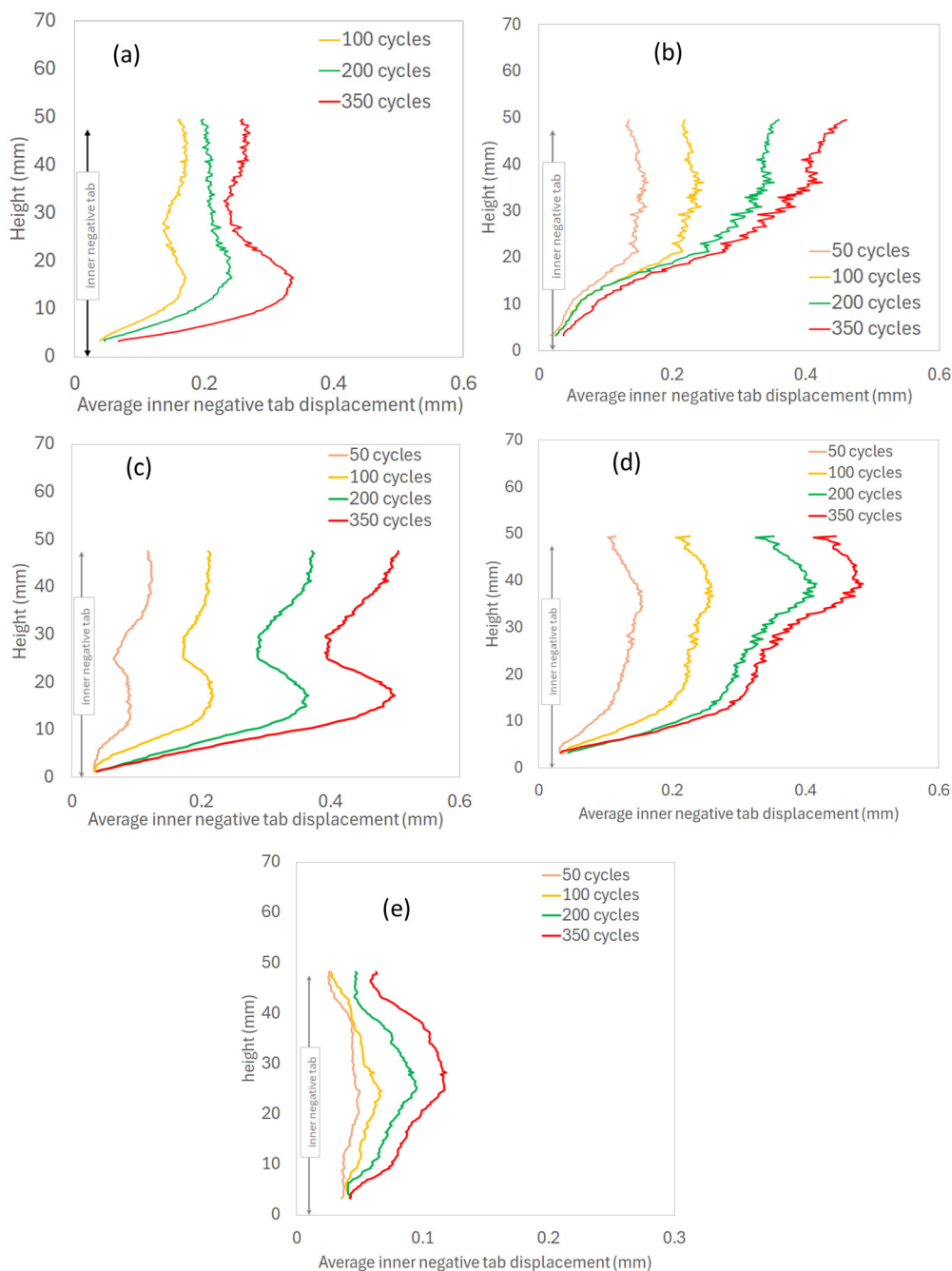


Fig. 14 Average displacement of the inner negative tab along cell height: (a) LIB09, (b) LIB15, (c) LIB18, (d) LIB20, (e) LIB25.



Outer layers. Within the outer layers, vertical bands of high tensile strains often initiate between the casing and the positive tab (and also opposite the positive tab depending on the cell), and spread radially from the casing to the inner core in the direction of the kinks-related strain concentrators (Fig. 10, 12c and S4, S6, S8, S10, S12c–15c). This is synchronised with vertical bands of tensile strains developing on both sides of the outer negative tab (Fig. 12c). Inside these bands, expansion takes place preferentially along the hoop direction. In most of the cells, the outer negative tab seems to act as an anchor point containing the jellyroll deformation (Fig. 12c and d, red stars). Around the positive and outer negative tabs, the compression is negligible in the inner/outer layers. On each side of the positive and outer negative tabs (Fig. 11, 12d and S5, S7, S9, S11, S12d–15d), the outer jellyroll is subjected to compressive bands, mostly along the hoop direction, extending to the inner core.

3.3. Correlation between expansion of the inner layers and displacement of the inner negative tab

The average tensile strain of the inner layers and the average displacement of the inner negative tab were both plotted against of the height of the LIB cells (Fig. 13 and 14). In LIB09, LIB20 and LIB25 cells, the expansion of the inner layers reaches a maximum at about 20–30 mm height and decreases towards the top/bottom. In LIB15 and LIB18, the expansion of the inner layers increases linearly up to 20–30 mm height, followed by a non-linear increase to the top. The inner negative tab displacement curves seem to correlate well with the inner layers expansion curves (see Table 3), suggesting a causal relationship between the inward expansion of the inner layers and the inner negative tab motion.

Moreover, a good correlation is found between the inner negative tab displacement and the expansion of the inner layers, both averaged across the height (Fig. 15). This suggests that the displacement of the inner negative tab alone could be a good indicator of the inward expansion/collapse of the jellyroll. In LIB25, the motion of the inner negative tab is 3–4 times smaller when compared with the remaining cells. This seems to be explained by the position of the buckled cathode layers relative to the inner negative tab. At BOL, the inner negative tab of LIB25 is sandwiched between the buckled layers around the inner core. During cycling, the inner layers of the jellyroll expand inward causing the inner negative tab to

Table 3 Pearson correlation coefficient values measuring the similarity between expansion of inner jellyroll and displacement of inner negative tab

Pearson coefficient	50 cycles	100 cycles	200 cycles	350 cycles
LIB09†	—	0.6	0.77	0.41
LIB15	0.93	0.92	0.98	0.96
LIB18	0.8	0.71	0.73	0.76
LIB20	0.19	0.7	0.75	0.8
LIB25	0.64	0.77	0.81	0.95

†The CT data of LIB09 at 50 cycles is missing and was ignored during the DVC analysis.

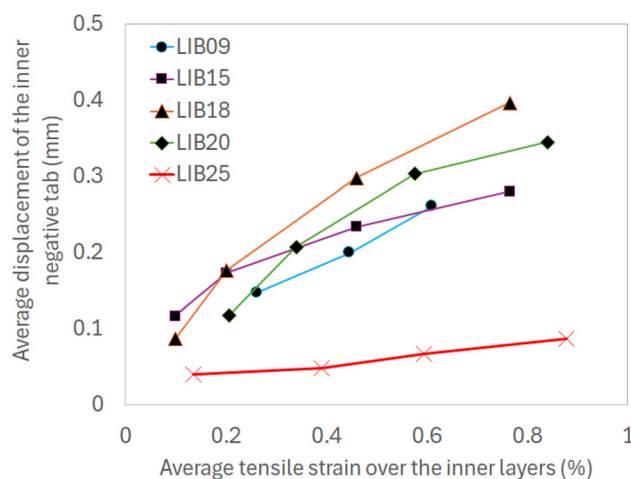


Fig. 15 Correlation between inner negative tab displacement (averaged across the inner negative tab height) and expansion of inner layers (averaged across the cylinder height).

deform and bend further (Fig. S4). Conversely, in the remaining cells, the contact surface of the inner negative tab is almost perpendicular to the buckled cathode layers at BOL causing the tab to be pushed away (Fig. 10, S6, S8 and S10).

3.4. Correlation between changes in jellyroll shape and buckling

Magnifying the shape changes of the jellyroll during cycling is very attractive as it allows to better identify the mechanisms driving core collapse. A circular shape of the inner jellyroll (blue region in Fig. 16a and 17a) was extracted from LIB20 and LIB25 cells at BOL and deformed by the DVC displacements (magnified by 10) obtained at each cycle. The results are illustrated in Fig. 16c and 17c. In LIB20, no apparent distortion was observed at BOL during inspection of the scan (*i.e.* no buckled cathode layers, Fig. 16a). Yet, during cycling, between the positive tab and core, the inner contour starts to progressively deform and deviate from a circular profile (Fig. 16c). This is accompanied by flattening (*i.e.* straight lines) and local distortion, especially after 350 cycles (Fig. 16c). This seems to correlate well with the presence in the same area of a small kink after 350 cycles visible in the CT section of the cell (Fig. 16b, red arrow). This result demonstrates that the mechanisms leading to wrinkling are consistent. In LIB25, buckled layers are already present at BOL in an area between the positive tab and the inner core (Fig. 17a). During cycling, the contour of the inner jellyroll undergoes flattening which exacerbates the buckling (Fig. 17c) due to the large hoop compressive strains and radial tensile strains (Fig. S4 and S5), as confirmed by the CT image (Fig. 17b).

4. Discussion

Our results link the complex mechanical behaviour of commercial cylindrical LIB cells to their internal structure during



ageing, revealing important conclusions about the mechanisms leading to core collapse.

4.1. Impact of geometric inhomogeneities

The DVC results revealed complex strain patterns during cycling, which exhibit dependencies on both radial and angular positions of the cell. Vertical bands of high expansion seem to always concentrate at an early stage around the positive tab and the innermost layers. The large tensile strains around the positive tab spread radially from the casing to the inner core in the direction of the defect-related strain concentrators. These defects can develop during formation (*e.g.*, buckled cathode layers in LIB25) or during cycling due to local distortion/flattening of the jellyroll (*e.g.*, small distortions

formed after 100 cycles in LIB20). In most of the cells, the inner core and the outer negative tab experience opposite effects during deformation. While the maximum expansion is observed around the inner core, the outer negative tab seems to limit the jellyroll deformation and influence the patterns of expansion/contraction found subsequently between the positive and outer negative tabs. This seems to be confirmed by Kok *et al.*,³⁵ who hypothesized that architectural anomalies such as the outer negative tab act as anchor points constraining 'jellyroll' movement, while other features like the free volume in the centre of the cell provide freedom for electrode movement. Other considerations regarding geometric inhomogeneities have been discussed by other authors.^{7,13,16,17,20,36} Pfrang *et al.*^{20,36} focussed on the role played by the positive

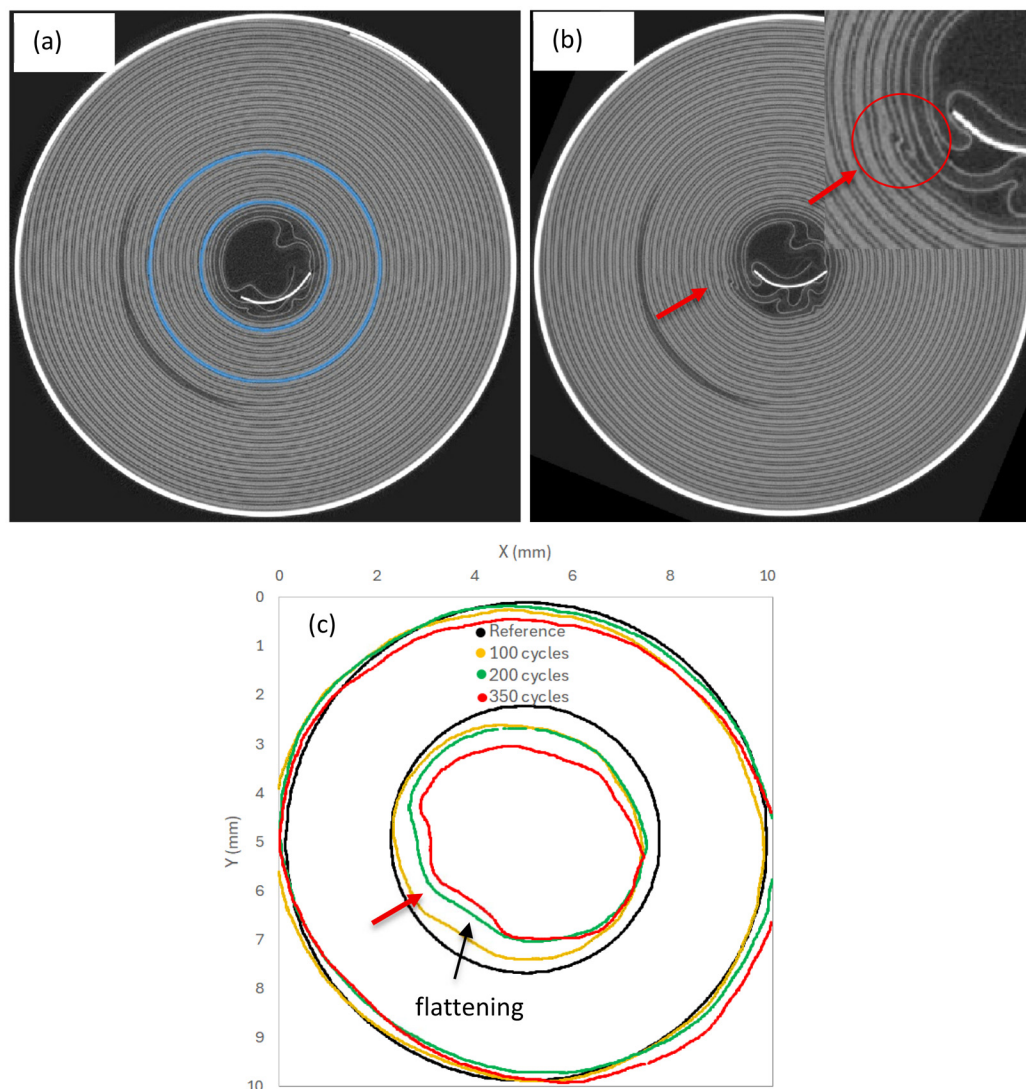


Fig. 16 Changes of jellyroll shape observed in LIB20: (a) CT section of the jellyroll before cycling at BOL (reference). (b) CT section of the jellyroll after 350 cycles where local distortion initiated around the innermost layers. (c) Evolution of the jellyroll shape versus number of cycles. For each CT scan, a binary mask of the jellyroll inner coils (blue region in a) was used to generate a surface mesh which was deformed by the DVC displacement field. The shape change has been magnified by 10 \times . During cycling, the inner contour starts to progressively deform and deviate from the circular dark profile. The jellyroll progressively flattens up to 200 cycles (dark arrow in c), creating a singularity from 350 cycles (red arrow in c), which seems to correlate with the local distortion observed in the CT scan (red arrow in b).



(cathode) tab and assumed that, being thicker than the cathode itself and interrupting the rotational symmetry of the jellyroll, additional pressure around this area is causing the jellyroll to relieve mechanically induced stress by deformation. Kok *et al.*⁷ raised the importance of consistent and accurate manufacturing processes with small defects in the jelly-roll being shown to act as nucleation sites for the structural degradation. The jellyroll will exploit any weaknesses in its internal structure, such as the buckled cathode layers, to relieve the stress. Bazinski *et al.*²² also showed that the cathode tab of a lithium-ion pouch cell always creates a source of Joule heating that is located at the junction of all the tabs within the cell, which could also explain the large strains observed around the positive tab. The presence of vertical bands during cycling was

also reported in a cylindrical commercial 18 650 battery cell by Jiang *et al.*²³ using a surface deformation technique, and was attributed mainly to the non-uniform contact between the internal jellyroll and the metal shell. This is yet another source of inhomogeneity that was not investigated in our study.

4.2. Wrinkling and buckling of the jellyroll

Our new method for tracking the changes in jellyroll shape allows to examine core collapse through a different lens. We demonstrated that the mechanisms leading to wrinkling and buckling can be reproduced and linked to the magnitude and direction of the local strains. During cycling, the innermost layers of the jellyroll deform and progressively experience flattening, which subsequently triggers (or exacerbates) buckling

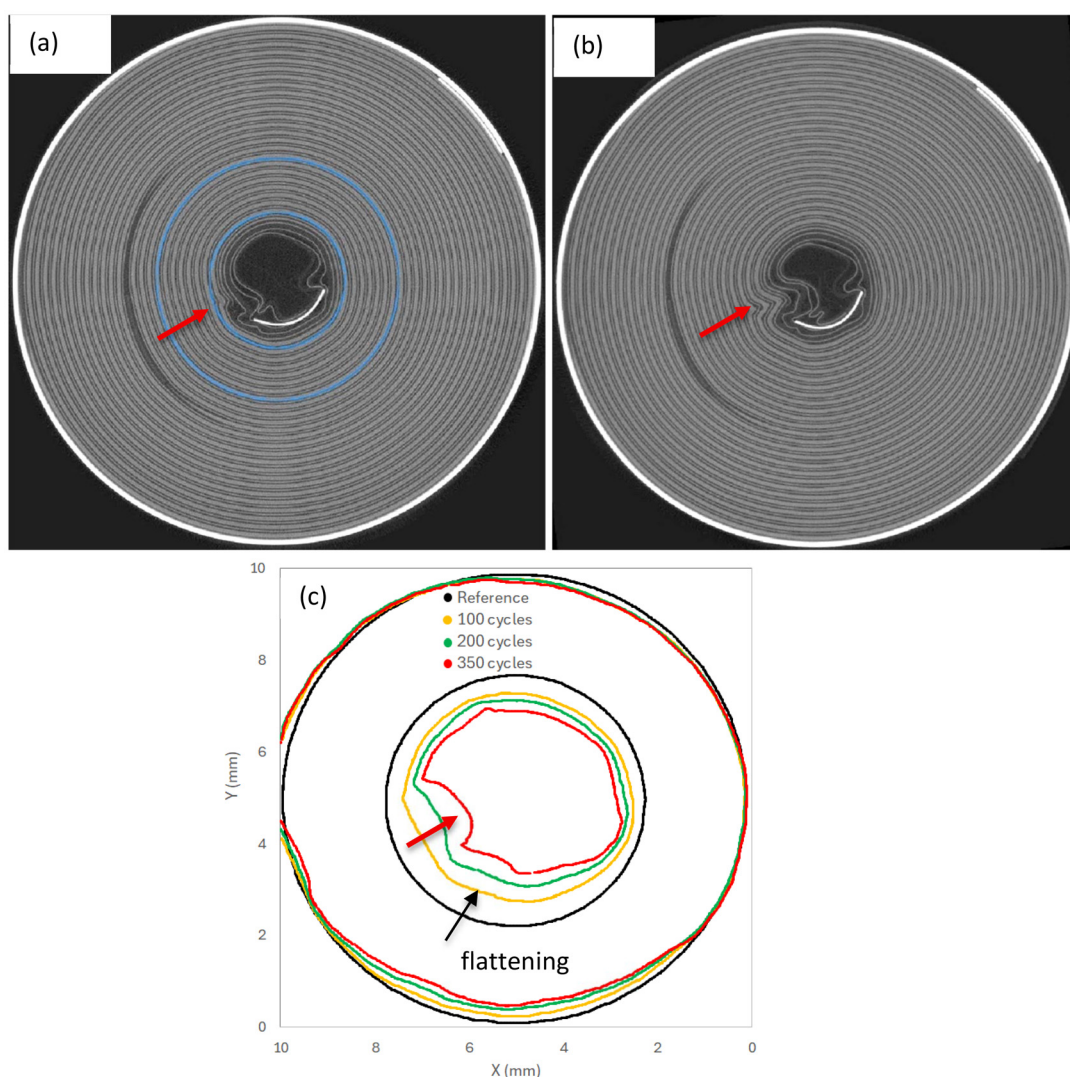


Fig. 17 Changes of jellyroll shape observed in LIB25: (a) CT section of the jellyroll before cycling (reference) where buckled cathode layers are present at BOL (red arrow). (b) CT section of the jellyroll after 350 cycles where exacerbated buckling is observed (red arrow). (c) Evolution of the jellyroll shape versus number of cycles. For each CT scan, a binary mask of the jellyroll inner coils (blue region in a) was used to generate a surface mesh which was deformed by the DVC displacement field. The shape change has been magnified by 10x. During cycling, the inner contour starts to progressively deform and deviate from the circular dark profile. The jellyroll progressively flattens up to 200 cycles (dark arrow in c), creating the conditions for buckling from 350 cycles (red arrow in c) due to the large hoop compressive strains.



depending on the condition of cell at BOL. This behaviour was discussed by several authors^{4,7,17,24,25} who speculated that the deviation from the circular profile of electrode layers could be acting as a precursor to inhomogeneities within the cell, triggering a buckling phenomenon within the electrodes. To the best of our knowledge, this is the first time that the magnitude and direction of the local strains are measured experimentally in 3D around the inner core. Around the innermost layers, large tensile strains were found to grow essentially along the radial direction, while large compressive strains develop along the hoop direction. It is therefore likely that wrinkling and buckling are caused by predominant compressive hoop stresses and large radial tensile stresses interacting simultaneously around the innermost layers. Based on mathematical modelling and reported causes of core collapse, Gelam *et al.*³¹ suggested that hoop buckling is the primary mechanism of electrode deformation leading to core collapse. Our experimental results seem to align with these conclusions and could be used to calibrate or validate numerical models.

4.3. Tracking the progression of core collapse through the inner negative tab

Our results reveal that the motion of the inner negative tab alone could be a good indicator of the progression of core collapse. A close relationship was found along the cell height between the motion of the inner negative tab and the expansion of the innermost layers. The motion magnitude depends on the orientation of the inner negative tab with respect to the direction of maximum inward expansion. When the inner negative tab was in the way of the progression of core collapse, *i.e.*, normal to the tab surface parallel to the inward expansion, the movement of the tab was at its maximum. This was the case for most of the cells (except LIB25) where the large tensile strains concentrated around the buckled cathode layers present at BOL. Reciprocally, when the normal to the tab surface was perpendicular to the inward expansion, the inner negative tab constrained the movement of the jellyroll, creating discontinuities and exacerbating the buckling. This was observed in LIB25 where the movement of the tab was at its minimum. In Ha *et al.*,³⁷ a methodology was proposed to evaluate core collapse initiation and progression by quantifying the void area in the core of the windings. Although the deformation of the inner negative tab was also proposed as a marker for core collapse progression, there was no detailed evaluation.

5. Conclusions

We have demonstrated that micro-CT coupled with digital volume correlation is a powerful technique to measure and track the 3D internal deformation taking place inside LIB cells. Our method was applied to five commercial cylindrical cells, selected with a diversity of buckling states at BOL, to study the progression of core collapse as a function of cycle number. The DVC results revealed important conclusions

about the core collapse mechanisms. During cycling, large tensile strains concentrate at an early stage around geometric inhomogeneities/defects like the positive tab, kinks, and negative tabs, which subsequently cause the stresses/strains to redistribute heterogeneously between the outer and inner layers. The mechanisms leading to wrinkling and buckling of the jellyroll could be reproduced during cycling and were found to be likely caused by distortion/flattening of the innermost layers, where large compressive hoop strains and radial tensile strains interact simultaneously. Our method could be used to understand the impact of cell design features on core collapse and provide experimental strain data to validate numerical models.

Author contributions

Conception and design of the study: K. M. and P. M. A. Acquisition of CT data: J. M., A. C., and P. M. A. DVC analysis and data analysis: K. M. and L. C. Interpretation of data, revision of the manuscript, final approval and agreement to be accountable for all aspects of the work: all authors. Drafting of the manuscript: K. M., P. M. A.

Conflicts of interest

This project was funded by Glimpse Engineering, Inc. and 3Dmagination Ltd. J. M., A. C., and P. M. A. all have employment and/or financial interests in Glimpse Engineering, Inc., which specializes in high-throughput CT for battery quality control. K. M. and L. C. have employment and financial interests in 3Dmagination Ltd, and are part of the team developing the XDVC Avizo software with Thermo Fisher Scientific where LR is employed.

Data availability

The data supporting this article have been included as part of the supplementary information (SI). Supplementary information: displacement and strain maps/graphs of LIB cells. See DOI: <https://doi.org/10.1039/d5eb00229j>.

Any further request for information should be directed to the corresponding author.

References

- 1 Y. Chen, Y. Kang, Y. Zhao, L. Wang, J. Liu, Y. Li, Z. Liang, X. He, X. Li, N. Tavajohi and B. Li, *J. Energy Chem.*, 2021, **59**, 83–99.
- 2 G. E. Blomgren, *J. Electrochem. Soc.*, 2017, **164**, A5019–A5025.
- 3 N. Nitta, F. Wu, J. T. Lee and G. Yushin, *Mater. Today*, 2015, **18**, 252–264.



- 4 S. D. Gelam, S. Maddipatla, C. Chicone and M. Pecht, *J. Power Sources*, 2024, **623**, 235471.
- 5 H. T. Reid, A. Fordham, L. Rasha, M. Buckwell, D. J. L. Brett, R. Jervis and P. R. Shearing, *Joule*, 2023, **7**, 2749–2759.
- 6 R. F. Ziesche, T. Arlt, D. P. Finegan, T. M. M. Heenan, A. Tengattini, D. Baum, N. Kardjilov, H. Markötter, I. Manke, W. Kockelmann, D. J. L. Brett and P. R. Shearing, *Nat. Commun.*, 2020, **11**, 777.
- 7 M. D. R. Kok, A. Jnawali, T. M. M. Heenan, T. G. Tranter, D. J. L. Brett, P. R. Shearing and J. B. Robinson, *J. Electrochem. Soc.*, 2023, **170**, 090502.
- 8 Y. Wu, S. Saxena, Y. Xing, Y. Wang, C. Li, W. Yung and M. Pecht, *Energies*, 2018, **11**, 925.
- 9 E. Lübke, L. Helfen, P. Cook, M. Mirolo, V. Vinci, O. Korjus, B. Fuchsbichler, S. Koller, R. Brunner, J. Drnec and S. Lyonard, *Energy Environ. Sci.*, 2024, **17**, 5048–5059.
- 10 P. Blazek, P. Westenberger, S. Erker, A. Brinek, T. Zikmund, D. Rettenwander, N. P. Wagner, J. Keckes, J. Kaiser, T. Kazda, P. Vyroubal, M. Macak and J. Todt, *J. Energy Storage*, 2022, **52**, 104563.
- 11 P. Blažek, O. Klvač, M. Šedina, O. Čech, M. Tkadlecová, Z. Stravová, T. Kazda, T. Zikmund, R. H. Schmitt and J. Kaiser, *J. Energy Storage*, 2025, **130**, 117436.
- 12 R. Carter, E. J. Klein, R. W. Atkinson and C. T. Love, *J. Power Sources*, 2019, **437**, 226820.
- 13 M. Spielbauer, M. Steinhardt, J. Singer, A. Aufschläger, O. Bohlen and A. Jossen, *Batteries*, 2022, **9**, 6.
- 14 A. Condon, B. Buscarino, E. Moch, W. J. Sehnert, O. Miles, P. K. Herring and P. M. Attia, *Data Brief*, 2024, **55**, 110614.
- 15 J. Min, A. Condon and P. M. Attia, *Batteries*, 2025, **11**, 73.
- 16 M. D. R. Kok, J. B. Robinson, J. S. Weaving, A. Jnawali, M. Pham, F. Iacoviello, D. J. L. Brett and P. R. Shearing, *Sustainable Energy Fuels*, 2019, **3**, 2972–2976.
- 17 A. Jnawali, M. D. R. Kok, M. Krishna, M. A. Varnosfaderani, D. J. L. Brett and P. R. Shearing, *J. Electrochem. Soc.*, 2023, **170**, 090540.
- 18 J. Jiang, X. Liu, X. Li and R. Yang, *J. Power Sources*, 2024, **621**, 235130.
- 19 A. Buljac, T. Taillandier-Thomas, L. Helfen, T. Morgeneyer and F. Hild, *J. Mech. Phys. Solids*, 2016, **96**, 550–571.
- 20 A. Pfrang, A. Kersys, A. Kriston, D. U. Sauer, C. Rahe, S. Käbitz and E. Figgemeier, *J. Power Sources*, 2018, **392**, 168–175.
- 21 T. Waldmann, S. Gorse, T. Samtleben, G. Schneider, V. Knoblauch and M. Wohlfahrt-Mehrens, *J. Electrochem. Soc.*, 2014, **161**, A1742–A1747.
- 22 S. J. Bazinski and X. Wang, *J. Electrochem. Soc.*, 2014, **161**, A2168–A2174.
- 23 W. Jiang, H. Li, S. Wang, S. Wang and W. Wang, *CCS Chem.*, 2023, **5**, 1308–1317.
- 24 P. Heugel, W. Märkle, T. Deich, O. Von Kessel and J. Tübke, *J. Energy Storage*, 2022, **53**, 105101.
- 25 L. Willenberg, P. Dechent, G. Fuchs, M. Teuber, M. Eckert, M. Graff, N. Kürten, D. U. Sauer and E. Figgemeier, *J. Electrochem. Soc.*, 2020, **167**, 120502.
- 26 Y. Ha, R. B. Licht, T. D. Bogart and K. M. Beers, *Front. Batter. Electrochem.*, 2024, **2**, 1287887.
- 27 K. Madi, G. Tozzi, Q. H. Zhang, J. Tong, A. Cossey, A. Au, D. Hollis and F. Hild, *Med. Eng. Phys.*, 2013, **35**, 1298–1312.
- 28 Y. Wan, S. E. Madi, K. Madi, J. Soete, J. Takahashi, S. V. Lomov and Y. Swolfs, *Composites, Part B*, 2025, **295**, 112220.
- 29 A. Buljac, C. Jailin, A. Mendoza, J. Negggers, T. Taillandier-Thomas, A. Bouterf, B. Smaniotto, F. Hild and S. Roux, *Exp. Mech.*, 2018, **58**, 661–708.
- 30 Y. Shi, B. Blaysat, H. Chanal and M. Grédiac, *Exp. Mech.*, 2023, **63**, 637–653.
- 31 S. D. Gelam, S. Maddipatla, C. Chicone and M. Pecht, *J. Power Sources*, 2025, **656**, 238104.
- 32 T. F. Morgeneyer, T. Taillandier-Thomas, A. Buljac, L. Helfen and F. Hild, *J. Mech. Phys. Solids*, 2016, **96**, 550–571.
- 33 H. Leclerc, J.-N. Périé, F. Hild and S. Roux, *Mech. Ind.*, 2012, **13**, 361–371.
- 34 A. Bartulovic, Z. Tomicevic, A. Bubalo and F. Hild, *Coupled Syst. Mech.*, 2022, **11**, 15–32.
- 35 M. D. R. Kok, J. B. Robinson, J. S. Weaving, A. Jnawali, M. Pham, F. Iacoviello, D. J. L. Brett and P. R. Shearing, *Sustainable Energy Fuels*, 2019, **3**, 2972–2976.
- 36 A. Pfrang, A. Kersys, A. Kriston, D. U. Sauer, C. Rahe, S. Käbitz and E. Figgemeier, *J. Electrochem. Soc.*, 2019, **166**, A3745–A3752.
- 37 Y. Ha, R. B. Licht, T. D. Bogart and K. M. Beers, *Front. Batter. Electrochem.*, 2024, **2**, 1287887.

